4.1 RECENT PROGRESS IN THE DEVELOPMENT OF DUCTILE-PHASE TOUGHENED TUNGSTEN FOR PLASMA-FACING MATERIALS — K. H. Cunningham, K. Fields, D. Gragg, F. W. Zok, (University of California, Santa Barbara); C. Henager, R. Kurtz, and T. Roosendaal (Pacific Northwest National Laboratory)

OBJECTIVE

The objective of this study is to develop the materials science of fiber-reinforced tungsten composites as candidates for plasma-facing components in future fusion reactors [1].

SUMMARY

Fracture testing was performed on notched and pre-cracked specimens of a W - 28w% Cu plate at room temperature and at 679K, as a follow-up to previous work. An order-of-magnitude toughness increase from that of monolithic tungsten was observed as a result of ductile Cu bridging. Pure W samples were consolidated from elemental powder using spark plasma sintering, achieving a maximum of 95.2% of the theoretical density. Commercially available tungsten wire was tested in tension, showing significant ductility and strength. The tungsten wire was plated with copper using electrodeposition, and continuing research will investigate methods of incorporating the Cu-coated W wire into a consolidated W matrix using spark plasma sintering. We expect the addition of ductile W wire to provide significant toughening compared to monolithic W, with the Cu coating preventing the wire from strongly bonding to the matrix.

PROGRESS AND STATUS

Background

Tungsten and W-alloys are the leading candidates for the plasma facing components because of their high melting point, strength at high temperatures, and low sputtering yield. However, W exhibits low fracture toughness and poor ductility. The ductile-brittle transition temperature (DBTT) typically ranges from several hundred up to ≈ 1000°C; and radiation hardening further elevates the DBTT [2-9]. Metallurgical approaches to toughen W-alloys, including Re alloying and severe plastic deformation (SPD), result in modest DBTT decreases [10-11]. However, they would be difficult or impossible to implement, due to high costs and implications to irradiation hardening (Re) or extremely complex processing demands (SPD) [12-14]. In contrast, W-composites toughened by a wide range of engineered reinforcement architectures are much more promising, especially those based on ductile phase toughening (DPT). There are many choices for ductile phases. Indeed, heavy metal commercial alloys, W-Cu-Ni-X, are composites. Copper is immiscible with W, does not form brittle intermetallic phases, and has low solubility in other elements like Fe. Thus copper coatings may be useful [17]. Limited studies of using fine-grained W-wire have had some success, and will be further studied. W-sheet or foils could also provide toughening given that a proper debonding behavior is established, perhaps by exploiting brittle intermetallic interface phases. Particle-toughened composites will also be considered. W-composite processing primarily will be by powder metallurgy that may involve use of commercial vendors, as well as coupon-size composite fabrication at UCSB using spark plasma sintering and at PNNL using hot- and cold-isostatic pressing and sintering. Powder processing will facilitate the exploration of a variety of ductile phases and more advanced approaches like functional grading.

Fracture Testing W-Cu Model System

Room Temperature Tests and Pre-Cracking (UCSB)

This research was conducted as part of this program and followed-up previous work prior to the proposal award. Specimens were prepared from a W-28 wt.% Cu plate obtained from Goodfellow. The nominal volume fraction of Cu particles is 50%. Initial fracture testing of the tungsten-copper composite began with manufacture of single edge-notched bend (SEB) specimens. The specimen geometry was 3.3 mm x 1.6 mm x 16 mm with the notch depth being 0.6 mm. The primary goal initially was to establish a method to produce pre-cracked fracture specimens for testing to measure ambient temperature fracture toughness, after which high-temperature testing could be conducted.

The first concept was to load the specimen monotonically in three-point flexure to introduce a sharp crack of known length. Since the crack growth in this material is bridged, the load-line deflection bears a complicated and *a priori* unknown relation to crack length, rendering conventional compliance correlation methods inadequate. Optical methods were used to measure and monitor crack growth during testing to establish not only final crack length, but also to plot the resistance curve behavior of the material. A number of optical systems were attempted, with the problem of specimen surface finish being a recurring issue. Conventional polishing techniques yielded a surface unsuitable for crack length measurements due to the preferential erosion of the copper, leaving raised “islands” of tungsten. Good results were obtained using 1500 grit sandpaper, which yields a uniformly flat surface, allowing good resolution of the crack formation and growth. In the end, an instrumented, long-distance microscope with oblique lighting and a digital camera provided good in situ imaging. It was found that monotonic loading of the SEB specimens did indeed produce stable crack growth, however, the level of plastic deformation and hinging of the specimen made this an unsuitable pre-cracking technique. However, the information obtained in these experiments yielded fracture data and proved the concept that the composite material exhibited rising R-curve behavior due to extensive crack bridging as illustrated in Figure 2.

Using the fracture data from the initial monotonic tests, a fatigue pre-cracking regimen was established to produce the desired fracture specimens. Successful pre-cracking was accomplished by high-frequency (80 Hz) fatigue in a displacement-controlled mode. Displacement-controlled fatigue was essential, since as the crack advanced, the load must decrease with the compliance, hence providing a stable, controlled crack growth mechanism. The crack length was monitored microscopically throughout pre-cracking. An example micrograph is shown in Figure 1.

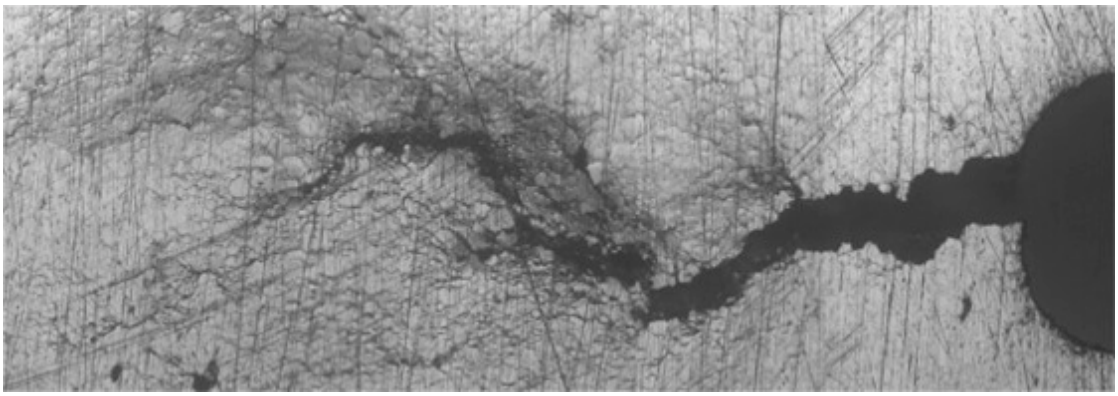

Figure 1. Stable crack growth from initially fatigued pre-crack.

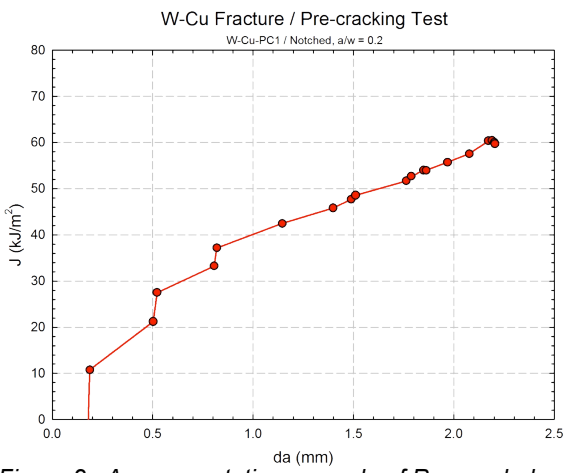

Figure 2. A representative example of R-curve behavior.

Once the ability to produce accurate, consistent fracture specimens was established, ambient temperature fracture tests were performed. There was some concern about a potentially large difference between surface crack length and through-thickness crack length. This led to extensive investigation into crack detection and monitoring techniques, including heat-tinting and use of dye penetrants. Heat-tinting proved of questionable use, since only the copper oxidized and changed color, leaving the apparent crack front essentially unchanged. However, this technique shows promise in revealing the individual tungsten zones to allow for microhardness testing of the tungsten itself. Dye penetrant proved a very useful method in understanding the formation and propagation of the crack front. By utilizing different colors at various stages of crack growth it is possible to visualize the length and shape of the crack, but also the level of bridging, since the copper ligaments are not marked while they are intact. A representative area of the fracture surface from specimen #7 is shown in the scanning electron microscope (SEM) image in Figure 3.

Table 1. Room temperature fracture data for notch and pre-cracked specimens.

Spec. #	a/w	K (MPa-√m)
1	0.20	$K_{el\text{-}pl} = 96$
2	0.20	$K_{max} = 24$
3	0.20	$K_{max} = 22$
4	0.20	$K_{max} = 24$
5	0.20	$K_{init} = 14$
6	0.32	$K_{el\text{-}pl} = 82$
7	0.49	$K_{el\text{-}pl} = 79$

Fracture testing of the pre-cracked SEB specimens at room temperature, along with the extensive microscopy, provided fracture toughness values (See Table 1), resistance curves (See Fig. 2 for example), and a wealth of understanding regarding the crack formation, propagation and bridging behavior in the tungsten-copper composite.

Elevated Temperature Tests (PNNL)

Preliminary experiments were performed to determine the effects of test temperature and displacement rate on ductile phase toughening of W-Cu composites. Single-edge notched bend (SENB) bars with nominal dimensions 3.38 mm width, 1.60 mm thickness, and 13.0 mm span were tested in three-point bending at room temperature (RT) and 679 K, which represent 21.6% and 50% of the homologous temperature for Cu, respectively. Based on an Ashby deformation mechanism map for pure Cu the higher test temperature places Cu in the power-law creep regime. Specimens were tested in both notched and fatigue pre-cracked conditions. Pre-cracking was performed at RT in displacement control at 80 Hz. Table 2 gives the measured dimensions, notch or crack depth, test temperature and displacement rate for each specimen.

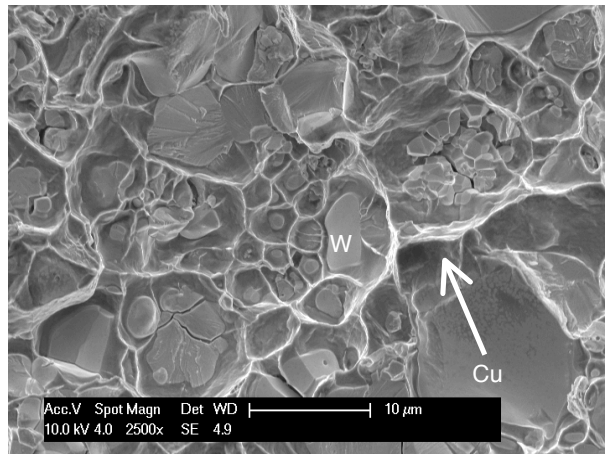

Figure 3. SEM image of fracture surface from SEB specimen #7. W grains show cleavage fracture and Cu shows failure by ductile bridging.

Table 2. Measured dimensions, notch or crack depth, test temperature, and displacement rate for room temperature (~293 K) and 679 K tests.

ID	Type*	Thick (mm)	W (mm)	S (mm)	a (mm)	T (°K)	Rate (mm/min)
11	N	1.610	3.345	13.335	0.643	293	0.2
12	N	1.595	3.317	13.335	0.671	293	0.02
13	N	1.593	3.325	13.335	0.648	293	0.002
14	N	1.604	3.299	13.335	0.597	679	0.2
15	N	1.585	3.329	13.335	0.632	679	0.02
16	N	1.597	3.182	13.335	0.52	679	0.002
8	PC	1.603	3.289	13.335	1.023	293	0.2
9	PC	1.595	3.317	13.335	1.219	293	0.02
10	PC	1.590	3.312	13.335	1.092	293	0.002
17	PC	1.617	3.318	13.335	1.296	679	0.2
18	PC	1.584	3.319	13.335	1.383	679	0.02
19	PC	1.584	3.269	13.335	1.309	679	0.002

**N = Notched, PC = pre-cracked*

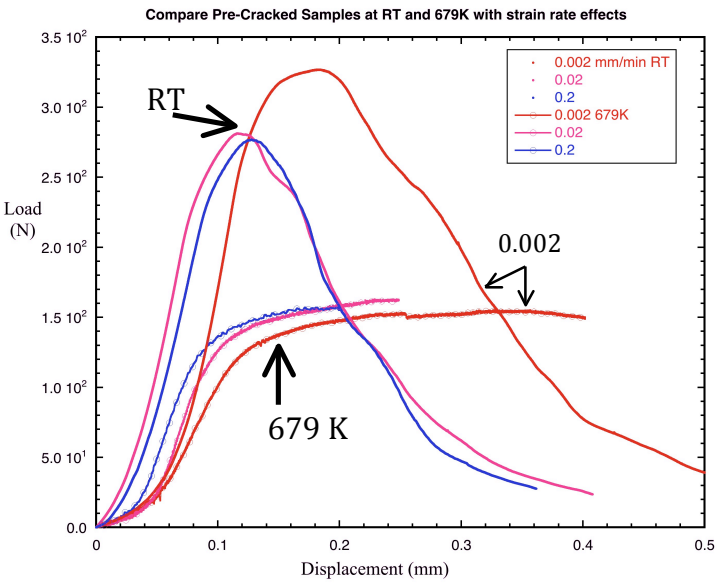

Figure 5. Displacement rate dependence of the load-displacement curves for pre-cracked tungsten-28 wt.% copper SENB specimens tested at RT and 679 K.

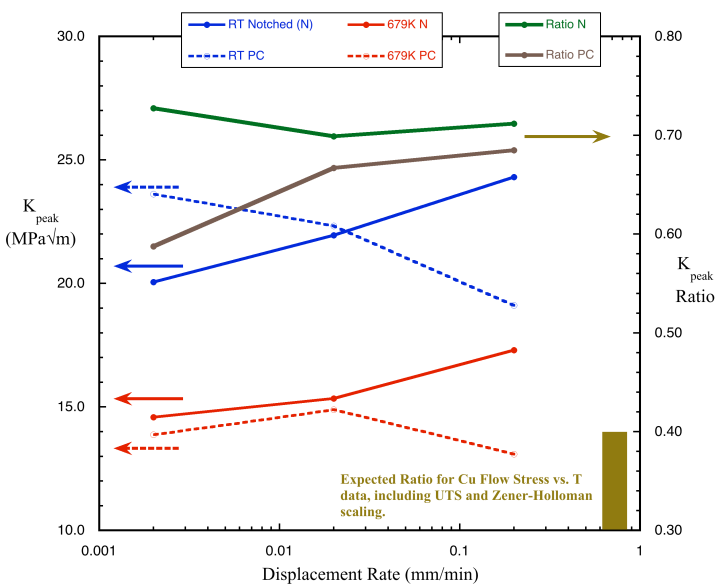

Figure 6. Peak load linear elastic stress intensity factor (left ordinate) versus displacement rate for notched (N) and pre-cracked (PC) W-28 wt.% Cu SENB specimens tested at RT and 679 K. The right ordinate plots the ratio K_{RT}/K_{679} at peak load.

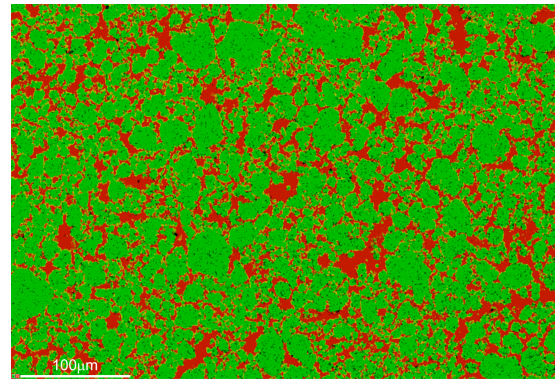

Figure 4. Elemental map of Goodfellow W-28 wt.% Cu plate showing W grains (green) surrounded by a network of Cu particles (red). The Cu particle areal fraction is between 31 and 38%.

The area fraction of Cu particles was determined from SEM image analysis indicating a range between 31 and 38% on the fracture surface. Figure 4 shows an elemental map derived from SEM energy dispersive X-ray spectroscopy. Tungsten is colored green and copper is red. The powder-processed material is best characterized as W grains surrounded by a Cu network.

Elevated temperature testing was performed in a tube furnace with a thermocouple directly contacting the specimen to control temperature to within ± 3 K. Displacement rates of 0.002, 0.02 and 0.2 mm/min were employed. Purified Ar gas flowed through the tube furnace to prevent specimen oxidation.

Load-displacement curves are plotted in Figure 5 for RT and 679 K tests as a function of displacement rate for the pre-cracked specimens. Note the results show a large effect from temperature, but a smaller effect from displacement rate. The total SENB specimen displacement increases markedly with decreasing displacement rate.

A working hypothesis for this composite material is that the fracture properties are determined by the ductile-phase mechanical properties, which in this case is the Cu phase. Since the Cu is in power-law creep at 679 K, it is not expected that the temperature dependence of the flow stress (yield or ultimate tensile strength) of Cu will be fully appropriate for scaling these results. Differences in specimen geometry, and notch or crack depths are accounted for, in an

approximate manner, by computing the peak-load linear elastic stress intensity factor, K_{peak}, for each specimen. These results are shown in Figure 6 as a function of displacement rate for each case, notched (N) and pre-cracked (PC) and RT and 679 K. The right hand axis in Figure 6 shows the K_{peak} ratio of the RT and 679 K values, which is a parameter that should reflect the temperature dependence of the Cu. Note the similarity in K-values for the N and PC cases.

It is evident that the measured K-ratio of about 0.7 is significantly higher than the ratio of Cu flow stress, which is indicated by the shaded box and ranges from 0.4 to 0.3. Therefore, not surprisingly, additional factors affect this K-ratio. One factor that needs to be included in a more rigorous analysis of these data is creep of Cu bridges restraining crack growth in W. The optical and SEM images shown in Figures 7 and 8 illustrate another factor, namely the width of the process or deformed and cracked zone ahead of the crack tip observed at 679 K. The process zone, a diffuse microcracked region, is more than twice as large at 679 K compared to RT. This will offset the expected K-ratio decrement due to decreasing Cu ultimate tensile strength. Creep of Cu bridges allows the Cu to absorb additional strain and the process zone growth distributes the stress and deformation over a larger volume. Both elevated temperature mechanisms act to offset the K-ratio decrement due to the higher test temperature.

Figure 7. Optical micrographs of tested RT (left image) and 679 K (right image) SENB bars showing an increase in the crack process zone (severely microcracked region) that develops during slow displacement rate testing.

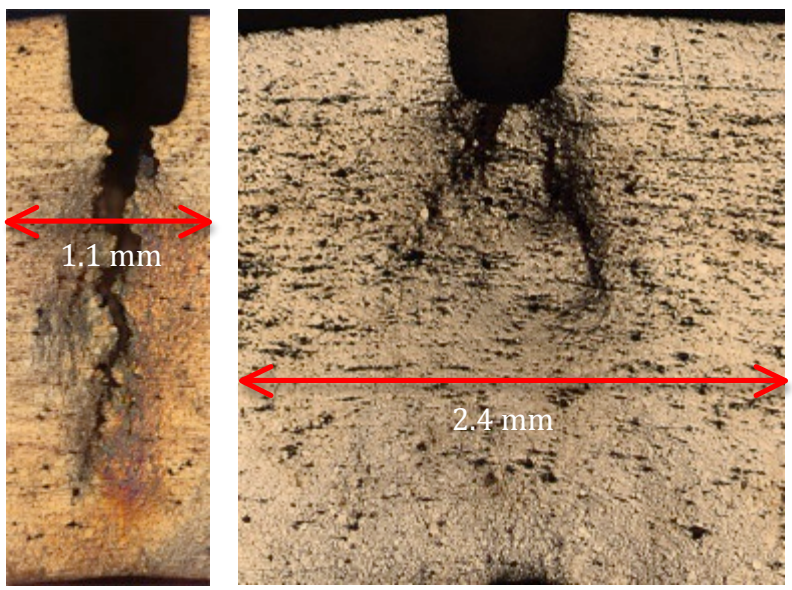

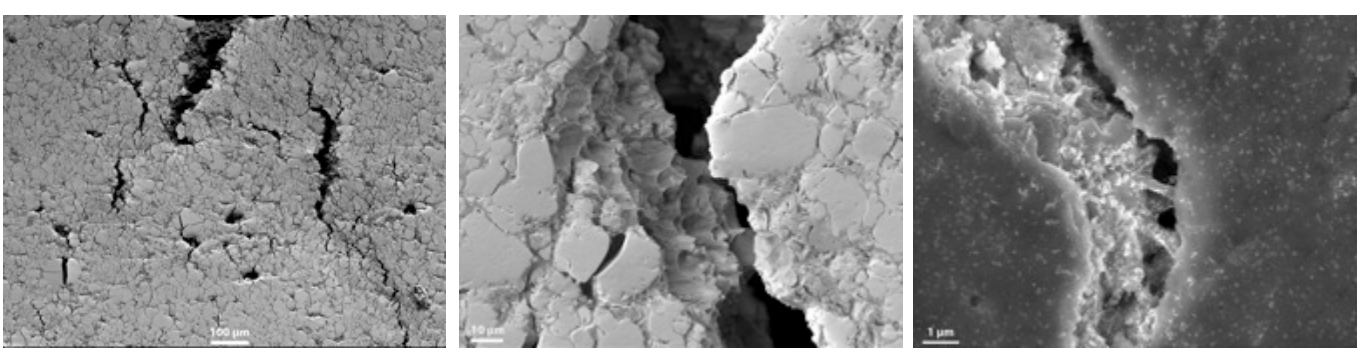

Figure 8. SEM image (left) of the crack process zone at 679 K. Cu bridges spanning the crack opening at RT (center) and 679 K (right). Plasticity in the Cu bridges is evident.

Processing W and W-Composites

Sintering of Pure Tungsten Disks

Two elemental tungsten powders, one of 4-6μm particle size and 99.95% purity (Stanford Materials Corp.) and the other of unknown particle size and purity (Aegis Tech.; assumed <4μm after cryogenic milling from 4-6μm powder) were used separately for this study. The powder was loaded under an argon environment into a 20mm inner-diameter graphite die with a layer of graphite foil between the powder and die (0.15" foil around circumference; 0.3" foil on faces). Two samples were prepared using 0.005-in. niobium foil, to reduce formation of tungsten carbide and potentially simplify processing [15]. For the Nb foil disks, one layer of foil was used for each face of the disk, and two layers were used around the circumference of the die. The powder was then consolidated by spark plasma sintering (Systeme GmbH, FCT Group) at various processing conditions summarized in Table 3.

After sintering, the tungsten disks were polished to remove any residual graphite. For the disks sintered at higher temperatures and longer dwell times, this exposed a cracked tungsten carbide outer layer. The disks were sectioned using a low-speed diamond saw (Buehler). One section per disk, cut along a chord of the circular face roughly 3mm from the edge, was mounted in thermosetting plastic. The visible cross-section of the disk was polished down to 0.5μm. An additional section no more than 5x5mm on the face was cut from the center of each disk to be used for density measurements.

The hardness of the consolidated tungsten was measured using a Leco M-400A microhardness tester. A series of 8-10 indents was made along the cross-section of each disk with a load of 500g. The density of each disk was measured using a helium pycnometer (MicroMeritics AccuPyc 1330) for the small center-cut sections. The grain size was roughly determined optically after etching in a 30% hydrogen peroxide solution for 10 minutes in an agitated bath [16].

On the disk sintered from the Aegis cryomilled powder, a second phase was visible in the tungsten matrix under optical microscopy. A section of the disk was cut and mounted in conductive thermosetting plastic for energy-dispersive x-ray spectroscopy (EDXS) analysis (FEI Sirion XL40 / Oxford Inca). The as-received Aegis powder was also mounted and analyzed with EDXS.

Table 3. Summary of SPS processing conditions and tungsten disk properties. Percent theoretical density (%TD) references 19.3g/cm^3 for pure single-crystal tungsten. All heating rates are 100°C/min approaching the maximum temperature. The relative density of the Aegis disk is not listed because of the presence of a second phase. (Nb) refers to the substitution of niobium foil as opposed to the standard graphite foil.

Powder	T(°C)	Dwell / cool t (minutes)	Density (g/cm^3)	% TD	Vickers hardness (dph)	Grain d (µm)
Stanford	1700	1/3	15.42	79.8	165.1 (6.1)*	6.09 (1.52)*
Stanford	1700	60/3	17.78	92.0	332.4 (9.6)	8.63 (3.02)
Stanford	1900	21/3	17.64	91.3	322.0 (9.2)	9.03 (2.78)
Stanford	1900	60/3	17.79	92.1	338.6 (7.3)	12.57 (5.80)
Aegis	1900	60/3	15.95	NA	495.8 (30.5)	29.78 (9.29)
Stanford (Nb)	1900	60/3	18.14	93.9	343.6 (6.8)	28.57 (6.48)
Stanford (Nb)	1900	5/3	18.39	95.2	224.6 (3.3)	

**(Standard deviation)*

The disk consolidated at 1700°C was relatively soft, which prompted extending the sintering time, after which the disks attained a higher density and hardness. The third disk was planned for a 60-minute dwell time, but the sintering machine's alarms were set off because the maximum piston travel setting was not high enough. The Aegis powder disk contained a tantalum oxide phase, as shown in Figure 9.

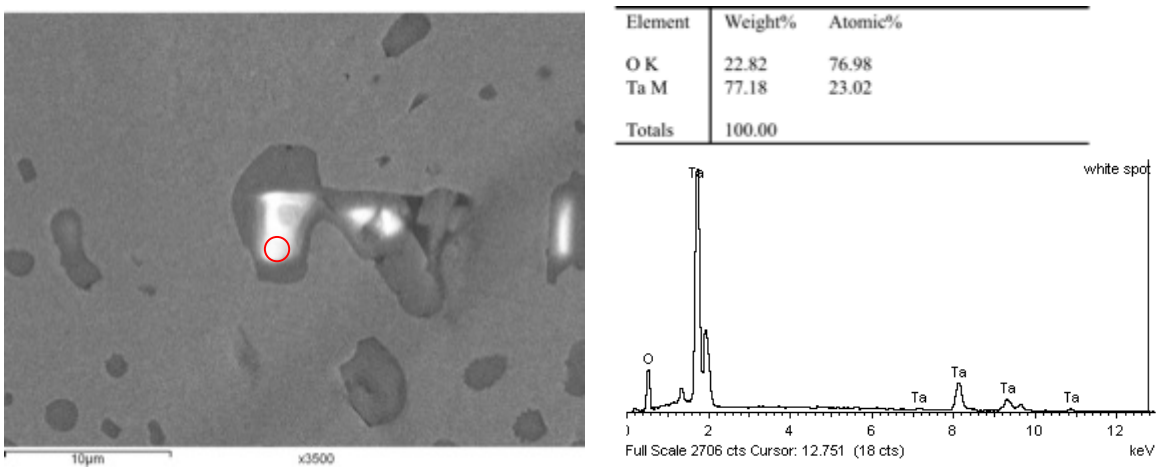

Figure 9. Oxidized tantalum phase in cross-section of consolidated Aegis powder disk. Data collected with Oxford Inca EDXS system. The elemental composition and spectrum shown for the spot highlighted in red on the SEM image. The scale bar is 10µm.

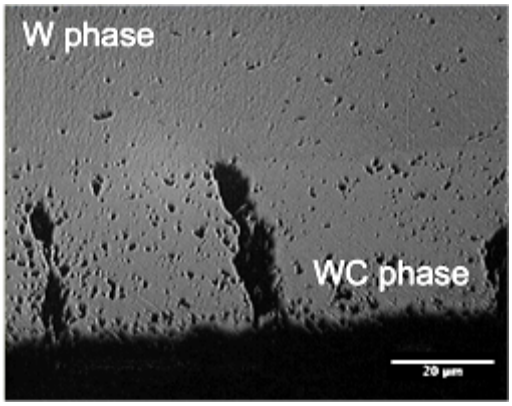

Figure 10. Optical micrograph of W-WC interface from disk 4 (Stanford, 1900°C, 60 min). Crack does not penetrate W matrix. Scale bar: 20µm.

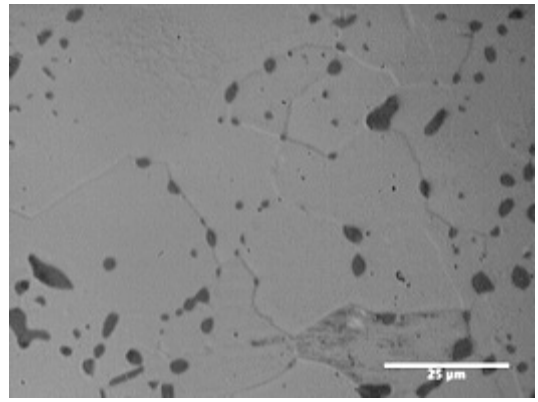

Figure 11. Optical micrograph of Aegis disk W matrix (lighter) with Ta second phase (darker) showing grain structure after 2.5-hr vibratory polish. Scale bar: 25µm.

All disks sintered with graphite foil except the first showed some amount of tungsten carbide on the outer surface. For the second disk (1700°C, 60 min), the WC was only present on a small area of the face of the disk; for the remaining three (1900°C), the entire disk was encased with a cracked WC layer. Figure 10 shows an optical micrograph with an example of cracks occurring only in WC.

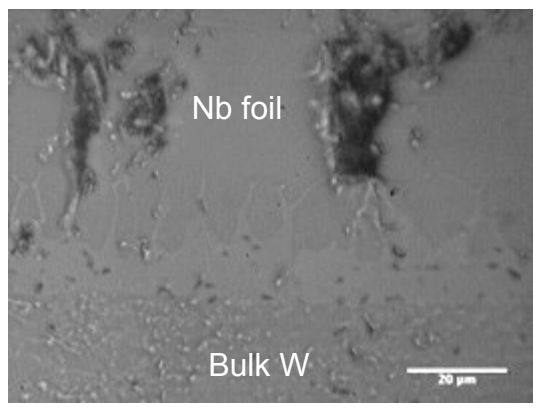

Figure 12. Optical micrograph of Nb foil at face of W disk showing diffusion of W into Nb. Scale bar: 20µm.

After a 2.5-hour vibratory polish of the Ta-contaminated disk, an apparent grain structure was visible under optical microscopy as shown in Figure 11. None of the other disks showed a visible grain structure after such a polish. The disks consolidated using Nb foil appeared under optical microscopy not to contain any WC. This will be confirmed using EDXS. An example cross-section of one disk at the face edge is shown in Figure 12.

Tungsten Wire Characterization

The concept of manufacturing a composite using copper-coated tungsten wire required the tensile testing of several candidate wires to quantify yield and ultimate tensile strength values to use in modeling. Tensile testing of 250- and 500-micron tungsten wire was performed using techniques and equipment developed for ceramic fiber testing. Several tests of each size wire were conducted to establish statistically valid results for tensile yield and ultimate tensile strength. Figure 13 shows typical engineering tensile stress-displacement curves for each of the three wire diameters, and Table 4 summarizes the wire tensile properties. If necessary, laser extensometry could be utilized to measure Young's modulus. The 15-micron diameter wire taxed the capabilities of the test equipment. However, preparing the test specimens by mounting them in rigid holders and then severing the holders once installed in the tensile machine proved successful with a 50% attrition rate. The tested specimens were examined microscopically to

verify cup-and-cone fracture to confirm uniform stress distribution in the wire (See Fig. 13). Unfortunately, measuring strain directly on the 15 µm wire is extremely problematic, therefore, modulus measurements are not planned.

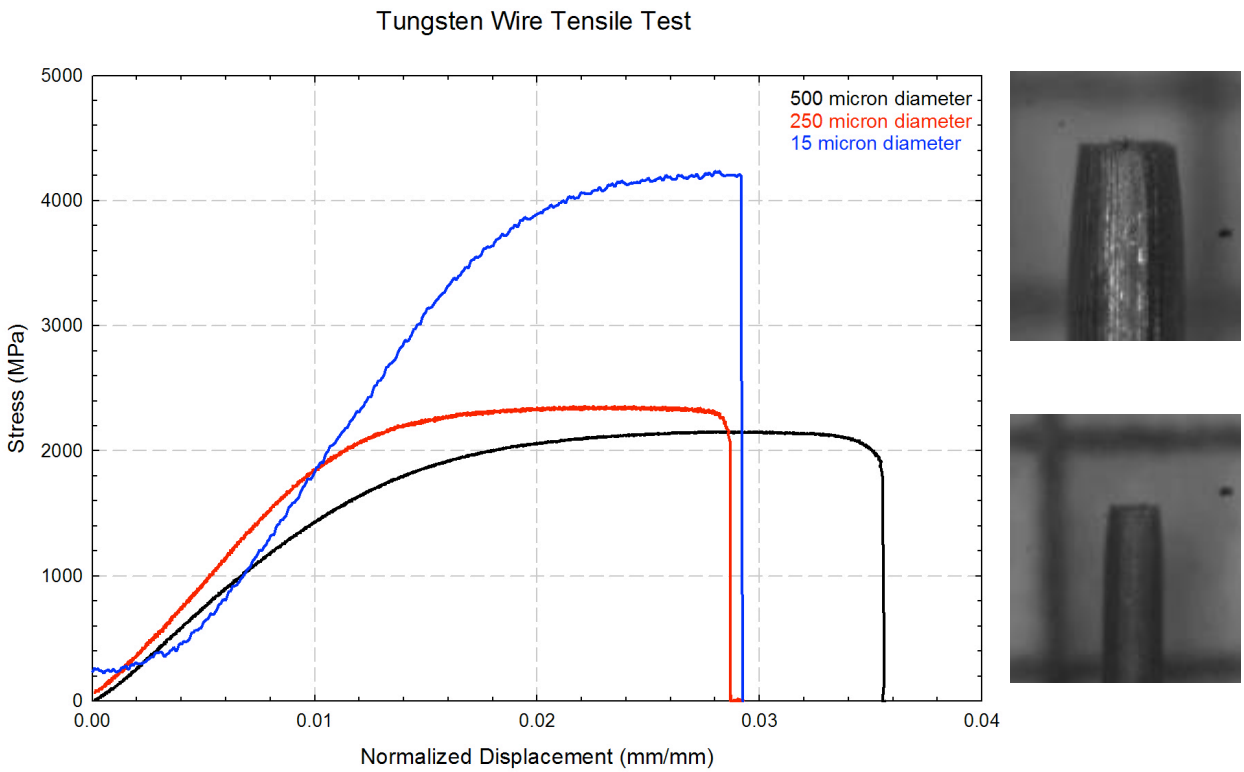

Figure 13. Typical test curves from three sizes of tungsten wire and optical micrographs of W wires after tensile test, showing necking before failure. Upper right: 500µm wire. Lower right: 250µm wire.

Plating Tungsten Wire with Copper

The initial process used to plate copper onto the tungsten wire is as follows: rinse and wipe wire with mineral oil to remove large particles; soak in ultrasonic bath in alkaline solution at 50°C for 15 minutes (solution: 0.1g sodium carbonate, 0.3g sodium borate in 19.6g water); plate in ultrasonic bath at 50°C under direct current, 162 A per m^2 of immersed wire (aqueous solution of 0.625M sulfuric acid, 0.4M copper sulfate, and 2 g/L urea) [17-19]. Plating for 1 minute did not result in full coverage of the wire with copper, as shown in Figure 14. Plating for 5 minutes resulted in a coating of maximum thickness 25µm, shown in Figure 15. Additional measurements are needed to quantify the variation in coating thickness, but the required thickness for achieving an appropriate interface once consolidated into a tungsten matrix is not known, but will be determined.

Table 4. Yield and ultimate tensile strengths of three sizes of tungsten wire.

Wire diameter (µm)	Avg. Yield Stress (GPa)	Average Ultimate Tensile Strength (GPa)
15	3.58	4.24
250	1.78	2.30
500	1.34	2.16

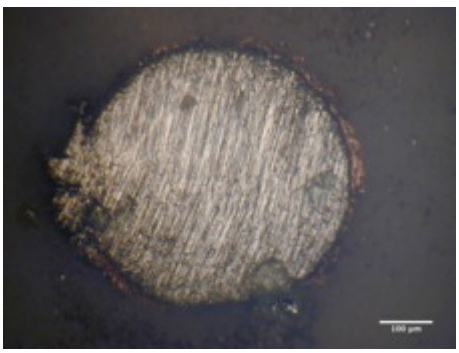

Figure 14. (Right) Optical micrograph of Cu-coated W wire after 1 minute of plating, showing gaps in coverage. Scale bar: 250µm.

Figure 15. (Left) Optical micrograph of cross-section of Cu-coated W wire after 5 minutes of plating, with a maximum coating thickness of 25µm. Scale bar: 100µm.

In an effort to increase the output of plated wire, a small-scale plating apparatus was constructed using a rectangular bath (w=3, l=5, h=10cm) with three bus wires running above the plating solution. Two of the bus wires were connected and run along the sides of the bath. Lengths of copper wire were hung from these buses to form the cathode. Tungsten wire was hung from the center bus to form the anode (See Fig. 16 for diagram). Eight lengths of tungsten wire were wiped with mineral oil and then hung from the anode bus so that approximately 8cm of each length was immersed in the plating solution. After plating at room temperature without agitation for 35 minutes, micrometer measurements indicated an average coating thickness of 30µm. Additional trials are required to establish a relationship between the wire preparation, plating process, and coating character.

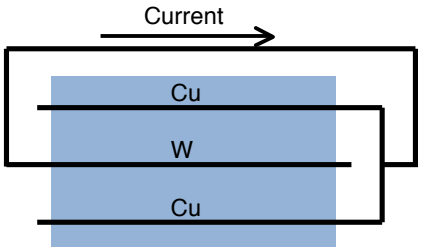

Figure 16. Top-down schematic of plating apparatus. The bare wire above the plating bath allows multiple lengths of current-carrying wire to be suspended within the bath. The W and Cu labels indicate the wire that hangs from each bus.

FUTURE RESEARCH

The next step in development of ductile-phase toughened tungsten composites is to combine the copper-coated wire study with the sintering study, and create composite materials to characterize. The largest challenge for this study is working with copper in the liquid phase, as the effective sintering temperatures for tungsten are well above copper's melting point. In order to create a composite, the copper must form a barrier between the tungsten wire and the tungsten matrix.

A poster on this research was presented in May 2013 at the 14th International Conference on Plasma-Facing Materials and Components for Fusion Applications, Forschungszentrum Juelich, Germany, in the poster "Ductile Phase Toughening in Tungsten-Copper Alloys at Elevated Temperatures."

REFERENCES

[1] C. H. Henager, et al., "*Ductile-phase toughened and fiber-reinforced tungsten for plasma facing materials,*" Proposal to the U.S. Department of Energy Office of Science, Fusion Energy Sciences. *Materials Solicitation with Focus on Structural Materials, Blanket First Walls, and Divertor Plasma Facing Components,* 2011.

[2] M. Rieth, et al., "*Review on the EFDA programme on tungsten materials technology and science," J. Nucl. Mater.* **417**, 463-467, 2011.

[3] R. A. Pitts, et al., "*Status and physics basis of the ITER divertor," Phys. Scr. Vol. T*, 014001, 2009.

[4] P. Mertens, et al., "*A bulk tungsten divertor row for the outer strike point in JET," Fusion Eng. Des.* **84** (7-11), 1289-93, 2009.

[5] A. Gervash, et al., "*Fabrication of a He-cooled divertor module for DEMO reactor," J. Nucl. Mater.* **367-370 B** (SPEC. ISS.), 1472-1475, 2007.

[6] M. Merola, et al., "*EU RD on divertor components," Fusion Eng. Des.* **75-79 (**Suppl.), 325-331, 2005.

[7] P. Mertens, et al., "*Clamping of solid tungsten components for the bulk W divertor row in JET- precautionary design for a brittle material," Phys. Scr. Vol. T* **2009 (**T138), 014032, 2009.

[8] A. Moslang, et al., "*Towards reduced activation structural materials data for fusion DEMO reactors," Nucl. Fusion* **45** (7), 649-655, 2005.

[9] M. A. Abdou, et al., "*On the exploration of innovative concepts for fusion chamber technology," Fusion Eng. Des.* 5**4 (**2), 181-247, 2005.

[10] B. Gludovatz, S. Wurster, A. Hoffmann, and R. Pippan, "*Fracture toughness of polycrystalline tungsten alloys," Int. J. Refract. Met. Hard Mater.* **28 (**6), 674-8, 2010.

[11] M. Faleschini, H. Kreuzer, D. Kiener, and R. Pippan, "*Fracture toughness investigations of tungsten alloys and SPD tungsten alloys," J. Nucl. Mater.* **367-370 A** (SPEC. ISS.), 800-805, 2007.

[12] T. Tanno, A. Hasegawa, J. C. He, M. Fujiwara, M. Satou, S. Nogami, K. Abe, and T. Shishido, "*Effects of transmutation elements on the microstructural evolution and electrical resistivity of neutron-irradiated tungsten," J. Nucl. Mater.* **386-388** C, 218-221, 2009.

[13] T. Tanno, A. Hasegawa, M. Fujiwara, H. Jian-Chao, S. Nogami, M. Satou, T. Shishido, and K. Abe, "*Precipitation of solid transmutation elements in irradiated tungsten alloys*," *Mater. Trans.* **49** (10), 2259-64, 2008.

[14] T. Tanno, A. Hasegawa, H. Jian-Chao, M. Fujiwara, S. Nogami, M. Satou, T. Shishido, and K. Abe, "*Effects of transmutation elements on neutron irradiation hardening of tungsten," Mater. Trans.* **48 (**9), 2399-402, 2007.

[15] I. Charit, et al., "*Fabrication of tungsten-rhenium cladding materials via spark plasma sintering for ultra high temperature reactor applications,*" U.S. Department of Energy (FY2009 NE-UP Program), 10/1/2009 to 9/30/2012.

[16] K. Williams, et al., "*Etch rates for micromachining processing,*" *J. Microelectromech. Syst.* **5** (4), 256-269, 1996.

[17] ASTM Standard B322, 1999 (2009), "Guide for Cleaning Metals Prior to Electroplating," ASTM International, West Conshohocken, PA, 2006, DOI: DOI: 10.1520/B0322-99R09, www.astm.org.

[18] ASTM Standard B482, 1985 (2008), "Practice for Preparation of Tungsten and Tungsten Alloys for Electroplating," ASTM International, West Conshohocken, PA, 2006, 10.1520/B0482-85R08, www.astm.org.

[19] I. S. Mahmoud, "Copper plating bath and process for difficult to plate metals." Patent 4,990,224. 5 February 1991.